Supplementary Information: Unravelling the spatial dependency of the complex solid-state chemistry of Pb in Old Master paintings using XRD-CT

Stephen W T Price, Annelies Van Loon, Katrien Keune, Aaron Parsons, Claire Murray, Andrew M Beale, J Fred W Mosselmans

Experimental

Sample preparation For XRD-CT, sample preparation was critical and required some micro-manipulation. An existing paint cross-section (#MH584_x35) prepared during treatment of the painting in 2005/06 was used. The sample had been taken from Homer's left hand that was covered with a whitish surface haze. The paint fragment (dimensions *c.*600 x 300 x 100 μm^3) was embedded as Easy Section (VWFecit, UK) using Poly-pol PS230 polyester mounting resin with M.E.K.-peroxide harder. The sample was ground to the level that all the paint layers were exposed, using a polishing machine with water as lubricant and silicon carbide (SiC) grinding paper. The final polishing steps were done using Micro-Mesh ® Sheets (Regular type, grades 1500 thru 12000). Prior to XRD-CT, the sample was characterized with optical/UV microscopy, and SEM-EDX. The mounting resin surrounding the paint fragment was removed as much as possible to get optimal results for XRD-CT. The resin block was glued face down with a carbon sticker on a polishing holder, and thinned on a polishing machine until the back of the paint fragment was exposed. Subsequently the thin slice was transferred onto Kapton tape. The mounting resin was further reduced with a scalpel knife. The Kapton tape holding the paint fragment was then glued with epoxy adhesive onto a 25mm-long, bevelled stainless steel rod, diameter 0.64 mm (MiTeGen), used for mounting of the sample in the beamline.

Light microscopy Light microscopy of the embedded sample was performed on a Leica DM2500 light microscope equipped with a Leica DFC490 digital camera. The layer build-up of the sample was examined at magnifications up to 500x, in bright field, dark field, and ultraviolet (UV-A) (Leica filter block 'A': BP 360/40, RKP 400, LP425).

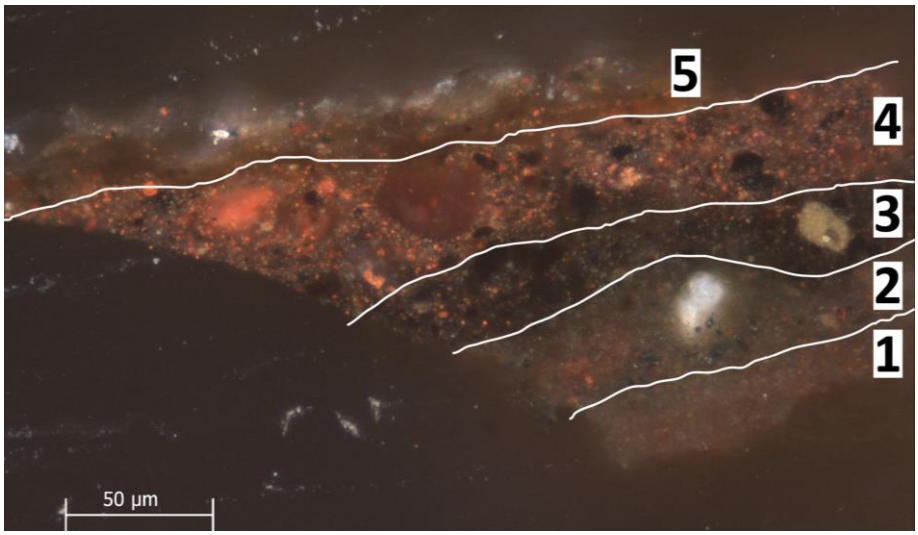

Figure S1: Light microscopic image of the Homer sample MH584_x35 showing: the layer build-up: (1) first orangey ground containing chalk and earth pigment (*c.*15 µm); (2) second beige-coloured (now darkened) ground containing lead white (saponified), little chalk, umber and black (*c.*20 µm); (3) dark brown undermodelling with bone black, earth pigment and dispersed lead (*c.*15 µm); (4) reddish paint with red earth, bone black, red lake, Kassels earth and dispersed lead (*c.*30 µm); (5) thin surface paint with smalt (discoloured), little fine red, black and lead-rich deposits (*c.*15 µm).

SEM-EDX Scanning electron microscopy studies in combination with energy dispersive X-ray analysis (SEM-EDX) of the embedded sample were performed at FOM Institute AMOLF, Amsterdam, using an XL30 SFEG high vacuum electron microscope (FEI, Eindhoven, The Netherlands) equipped with an EDX system with spot analysis and elemental mapping facilities (EDAX, Tilburg, The Netherlands). Backscattered-electron images were recorded at 20 kV accelerating voltage, at a 5 mm eucentric working distance and a spot size of 3, which corresponds to a beam diameter of 2.2 nm with current density of approximately 130 pA. EDX was done at a spot size of 4, which corresponds to a beam diameter of 2.5 nm and

current density of 550 pA, to obtain a higher count rate. Mapping settings were 256 x 200 matrix, 200 µs dwell time, and 17 µs amplitude time. The sample was carbon coated using a CC7650 Polaron carbon coater and carbon fibre (Quorum Technologies, Newhaven, East Sussex, UK) prior to analysis to improve surface conductivity.

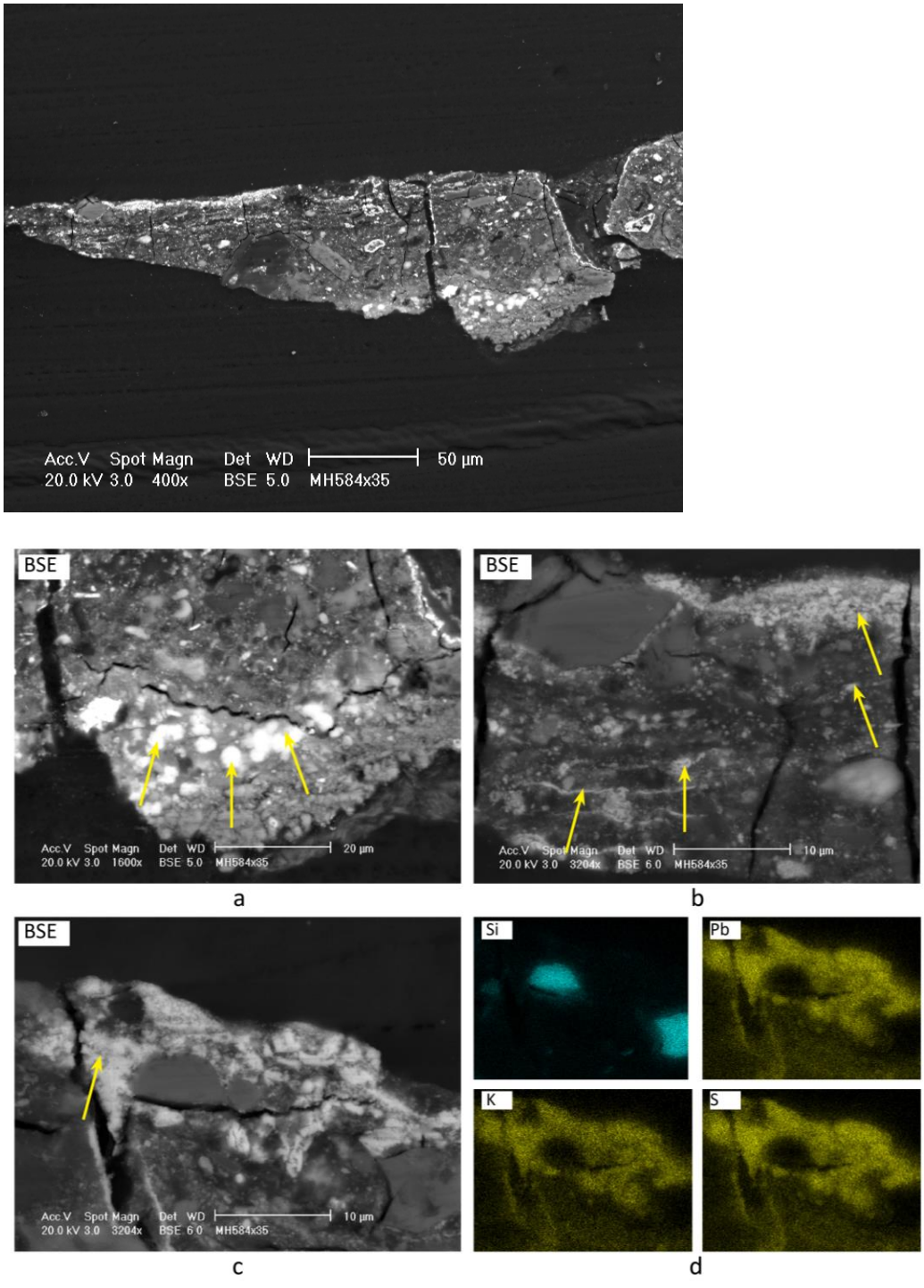

Figure S2: SEM-EDX detail images of the *Homer* sample MH584_x35 showing: a) The dissolution and saponification of lead white in the upper ground, as can be recognised in the SEM backscattered-electron (BSE) images by its less dense amorphous appearance (see arrows), in contrast to well-defined, highly scattering intact lead white particles typical of Dutch stack-processed lead white. All the small particles have reacted away. while the edges of the large particles are also dissolving; b) Highly scattering, lead-rich horizontal migration fronts as well as many dispersed particles are visible in the dark paint matrix; c) detail of the highly scattering, lead-rich surface crust integrated in the paint structure and surrounding the smalt particles, and d) corresponding EDX maps of Si (indicative of smalt), Pb, K and S (present in the lead-rich surface deposits).

X-ray diffraction computed tomography (XRD-CT)

X-ray data were recorded at beamline I18 of Diamond Light Source operating with a Si(111) double crystal monochromator, with the X-ray beam focused to a 2 μm x 2 μm (FWHM) spot on the sample using Kirkpatrick-Baez mirrors[1]. XRD-CT data was collected using an incident X-ray energy of 12.9 keV with a Photonic Sciences CMOS based X-ray imaging detector. The photon flux at this energy is approximately 1 x 10^{12} photons s^{-1} (of which ca. 45% is transmitted through the sample, using the attenuation coefficient of $PbSO_4$). The sample was stepped across the beam in a translate-rotate data collection scheme, with an XRD imaged collected at 2 μm intervals with a collection time of 2s/pixel, taking 4-6 hours per slice (due to the step-scanning of the stage and inclusive of detector readout time). Data were collected over two beamtime sessions. In the first, typically 61 translation steps at each rotation angle and 103 rotations (in 3.5° steps) were used – the exact number of translations was dependent on sample width. In the second, finer rotation steps of 2° were used to cover the same angular range.

Data were calibrated, processed and reconstructed using the Savu tomography reconstruction pipeline[2] by the filtered back-projection method[28] with Shepp-Logan filtering and linear interpolation. The final dataset is a 3D datastack; having 2 spatial axes (x, y) and the 3rd axis (z) being the reconstructed pattern (2θ, d-spacing etc). Each pixel consists of an XRD image that was calibrated (using a LaB_6 reference material), and then remapped from Cartesian to polar coordinates. A mean trimmed filter (Figure S3) was applied to the remapped images[3], resulting in a diffraction pattern associated with each pixel. The filter (which trimmed the top/bottom 10% intensity per angular step in the diffraction image) was required as the paint fragments contain multiple crystallites with dimensions comparable to those of the X-ray beam. These single crystals produce "hot-spots" in the sinogram that, when reconstructed, result in streak artefacts in the reconstructed XRD-CT images. Full technical details on the mean trimmed filter method can be found in reference [3]. The removal of these spots firstly enables clearer identification of the spatial distribution of the phase, and secondly provides suitable data for performing principle component analysis (PCA) and cluster analysis (CA), which were performed on the reconstructed XRD-CT data using Mantis[4].

The azimuthally integrated and mean trimmed filtered reconstructions was used as the input data for the PCA over the range 1.75 to 5.0 Å. The PCA orthogonalised and noise-filtered the data such that the cluster analysis was able to classify the data into regions with similar patterns, i.e. with similar pattern shape and/or intensity. The number of clusters identified for each dataset was dependent on the PCA results. Full details on the manner of calculation of eigenspectra and eigenimages are detailed in reference [4]. Mantis is written in Python and uses the scipy.cluster package to k-means cluster the data. A map of these regions was generated, along with summed diffraction patterns from each region. The XRD data were fitted using Topas v4.2 for phase identification[5]. It was possible to confirm the location of certain phases by the presence of unique reflections (e.g. Calcite at 3.04 Å d-spacing, detailed in Table S1).

The XRD fitting procedure, using least squares minimization, was systematically applied across all samples/clusters, using the fewest parameters possible, and excluding all phases that did not contribute to (or improve) the quality of fit. If an incorrect phase were to be included in the fit, it would result in a complete misfit (i.e. a straight line) and not be incorrectly attributed to the sample. Whilst the measurement conditions were optimised for the sample, it is not an "ideal" sample for XRD, with poor crystallinity, varying crystallite sizes and multiple phases all potentially present within a single pixel, in addition to the necessity to filter out the signal for large crystallites. Therefore the noise level in this data is greater than would be expected from a dedicated high resolution powder diffraction beamline at a synchrotron for an "ideal" sample, and is the main contributing factor to the residual fraction in the phase identification fits.

Discussion on mean trimmed filter applied to XRD-CT data

The paint fragments are highly complex, with multiple crystalline Pb phases present throughout. Some of these crystallites are much smaller than the X-ray beam size (<2 μm) and numerous, resulting in diffraction rings that can be imaged at multiple projections. Once the data is calibrated and azimuthally integrated, data resulting from diffraction rings results in a continuous sine wave which can be reconstructed (Figure S3). Some of the crystallites, however, were of a similar size, or larger, to that of the X-ray beam. Consequently, these crystallites will only generate diffraction spots at certain orientations to the beam, resulting in interrupted sine waves that when reconstructed have significant streak artefacts (Figure S3).

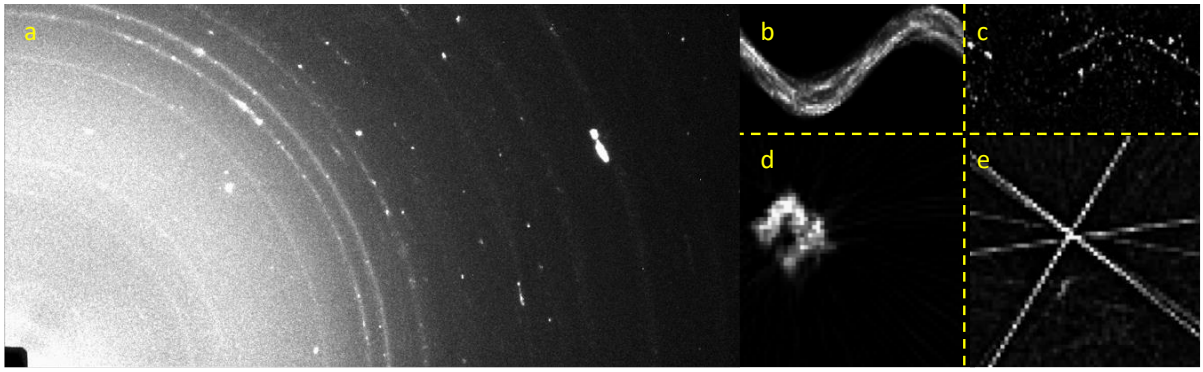

Figure S3: a) an example diffraction image showing rings and spots. Sinograms (b,c) and corresponding reconstructions (d,e), for diffraction signals originating from rings (b, d) and spots (c, e).

During principal component analysis, these streak artefacts deviate the most from the average signal and therefore the majority of components identified are streak artefacts, with only a few components corresponding to the signal that constitutes the majority of the sample. Removal of the streak artefacts by using a mean trimmed filter[3] in the processing step results in the PCA identifying regions of the sample with distinctly different diffraction patterns, rather than highlighting single crystal hot spots, that are then identified via the cluster analysis.

Summing the XRD patterns over all pixels in the XRD-CT reconstruction gives an averaged pattern of the sample, similar to that from bulk XRD (Figure S9). This "bulk" pattern however is much more complicated to fit due to the large number of phases present (approximately double that from the regions identified by tomography), with contributions from minor phases lost, as with lab based XRD, and so it is not possible to unambiguously identify and assign all phases present.

The cluster analysis provides a straightforward means to identify regional variations in the composition of the sample without having to directly interpret the XRD patterns. In this case, the Rembrandt fragment has a striated structure: a base layer, an intermediate layer, and an upper layer. Within these layers, small inclusions that stand out. The corresponding absorption images reveal what appears to be either delamination of the paint layers, or small voids.

It is important to highlight that the mean trimmed filter applied to the data only filters the highest intensity signals, but leaves the majority of the signal (so it does not artificially remove a peak that would lead to errors in peak indexing). Whilst peak position is unaffected, peak intensity is, and so quantitative analysis, such as Rietveld refinement, is not possible. However the patterns can still be matched to a large database to identify the phases present, since these spatially resolved regions contain fewer phases and are therefore easier to interpret. Many of the lead phases have very similar if not identical peak positions. Phase identification using Topas (Figure 2, S3 and S4) means that it is possible to identify which peak(s) is unique to each phase, and can therefore be used to generate maps of each individual phase present in the paint. This is true even for some of the more complex phases, notably the lead soaps which have very large large monoclinic unit cells.

It is important at this stage to differentiate information obtained from the cluster analysis from maps of individual phases. Since many of the phases have some large crystallites present, these can exhibit streak artefacts in the reconstruction that extend beyond its true location in the sample. Viewing a map of such an occurrence (e.g. calcite for either sample) it is easy to interpret where phase is actually located. However, in some instances (e.g. leadhillite or hydrocerussite in the Rembrandt sample), it can be less clear. It is in these cases where the limitations of the cluster analysis are reached. Since the pattern associated with each cluster is the sum of the pattern from every pixel it encompasses, if a streak artefact from a large crystal elsewhere in the sample intrudes in this region, the contribution from that phase will be included in the summed pattern. Hence in the cluster associated with the base layer of the paint fragments, whilst it is primarily calcite (and this is born out in the individual phase maps), the summed pattern associated with the cluster contains contributions from hydrocerussite and other phases (Figures S4-6). Both approaches to interpreting the data are complementary, the cluster analysis simplifies the initial interpretation of the data, such as identification of the phases present and visualisation of the structure, whereas the individual phase maps, whilst harder to initially assign, provide a definitive location for each phase.

Limitations of the reconstruction method

Filtered back projection is limited by noise and streak artefacts. The use of several filters (ramp, cosine, hamming) were investigated, with the Shepp-Logan filter chosen giving the sharpest reconstruction. Linear interpolation was used as it was much faster than cubic but did not significantly impact the noise levels in the reconstructed image (given that ca. 4000 angular bins were reconstructed per slice). With regards to reconstructed signal extending beyond the sample boundaries (streak artefacts), this can happen when the number of projections is undersampled, whether due to too coarse a rotation step, or when the data in the sinogram is not continuous – as occurs with single crystal diffraction. After the use of the mean trimmed filter, very few streaks extended beyond the sample boundary. With faster data collection the number of projections per sample can be increased to improve the sampling rate and therefore reduce some noise, however the problem of single crystal diffraction would still remain. Iterative methods could be used instead of FBP to reconstruct the data; whilst these would take longer, they may result in a reduction in noise, however the streak artefacts would remain due to the non-continuous nature of the features in the sinograms.

Table S1**.** Reaction products identified in the *Homer* sample by XRD-CT. The chalk layer starts approximately 80 µm beneath the surface of the paint. Note Pb is present as Pb^{2+} in all phases.

Phase	Formula	Pb:S ratio	Range of depth of phase / µm[a]
Palmierite	$K_2Pb(SO_4)_2$	0.5	0 - 30
Anglesite	$PbSO_4$	1	0 - 30
Lanarkite	$Pb_2(SO_4)O$	2	20 - 50
Leadhillite	$Pb_4SO_4(CO_3)_2(OH)_2$	4	15 - 50
Cerussite	$PbCO_3$	n/a	30 - 40
Hydrocerussite	$Pb_3(CO_3)_2(OH)_2$	n/a	45 - 60
Lead palmitate[b]	$PbC_{32}H_{62}O_4$	n/a	12 - 75

[a] Range of depth of phase is based on slice 1; [b] Representative of all lead soaps.

Table S2: D-spacings used to identify phase locations. NB no unique peak could be assigned to lead azelate – all peaks had overlap with at least 1 other phase (see plot – patterns not available for lead palmitate or lead azelate; CIF files we used for the Topas inputs).

Phase	**D-spacing (Å)**
Anglesite	2.78
Calcite	3.04
Cerussite	1.75 / 3.59
Hydrocerussite	4.25
Lanarkite	3.70
Lead azelate*	---
Leadhillite	2.85
Lead palmitate	4.12
Palmierite	3.11

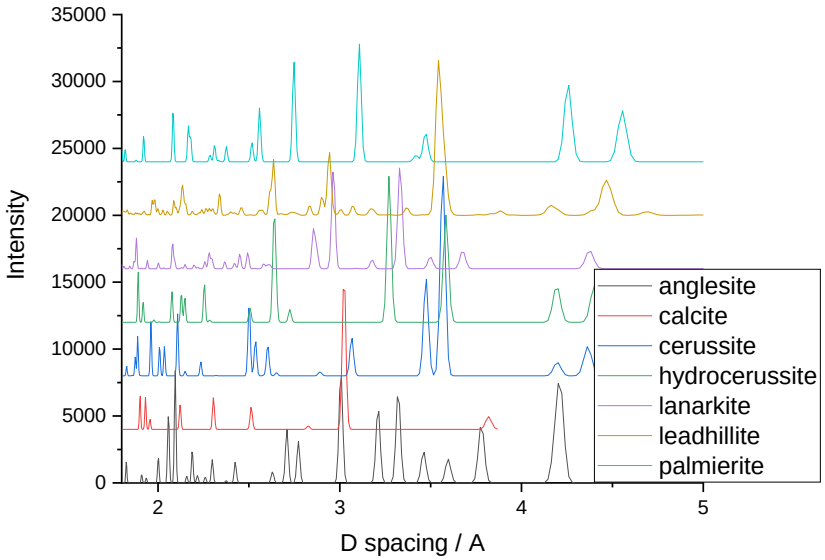

* Lead azelate was confirmed through the phase identification in Topas but a unique reflection was not present to be used for spatial resolution

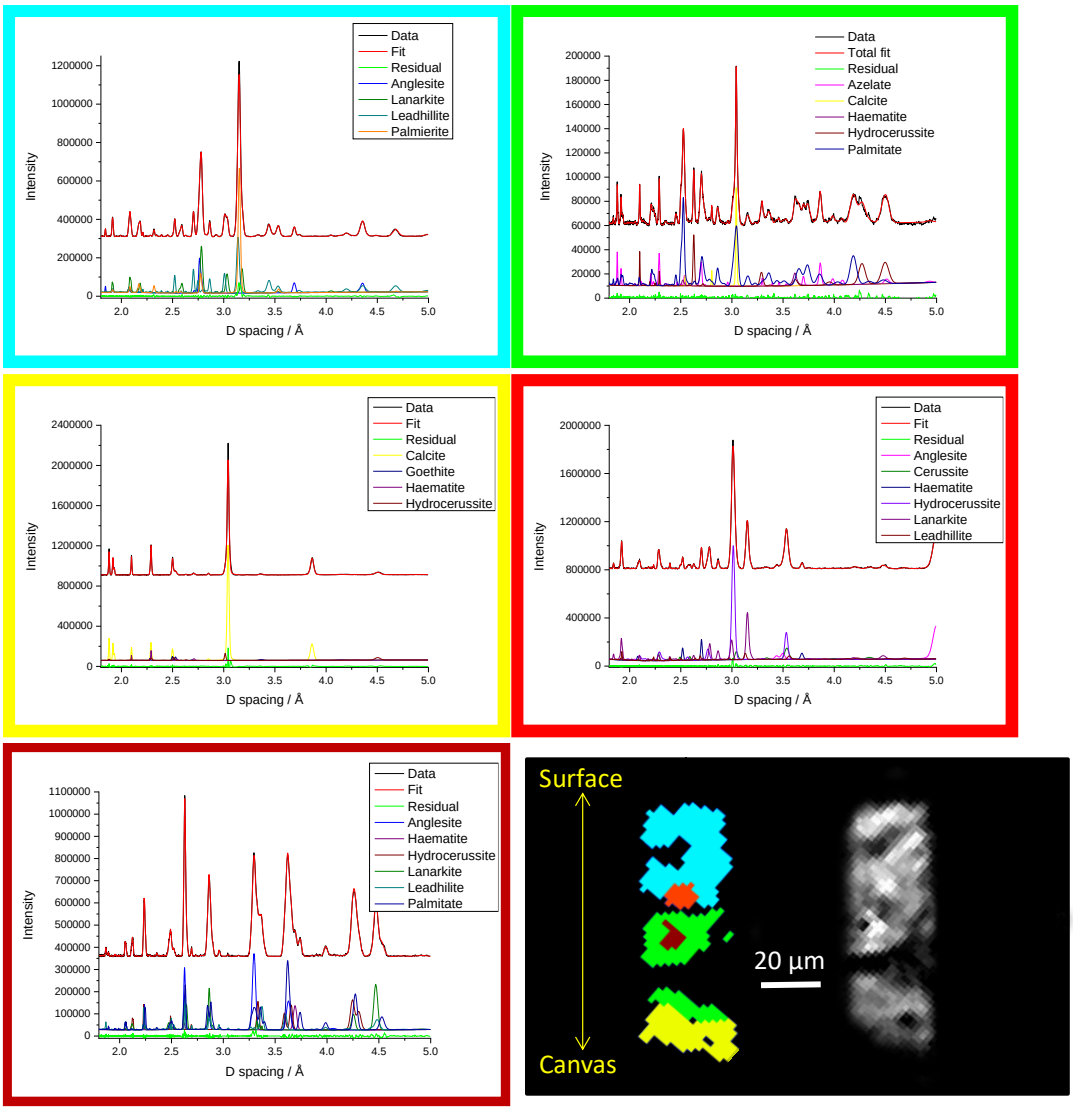

Figure S4: Cluster analysis of XRD-CT slice 1 (bottom middle), and absorption-CT (bottom right) of second tomogram location and diffraction patterns associated with each cluster (the colour of the box around the plot corresponds to the colour of the cluster in the XRD-CT image). Within each plot associated with a cluster, all phases have been assigned a unique colour: anglesite (light blue line), palmierite (orange line), lanarkite (green line), leadhillite (dark green line), calcite (yellow line), lead palmitate (blue line), hydrocerussite (brown line), goethite (dark blue line), haematite (purple line), lead azelate (pink line). Data (black line), fit (red line), residual (light green line).

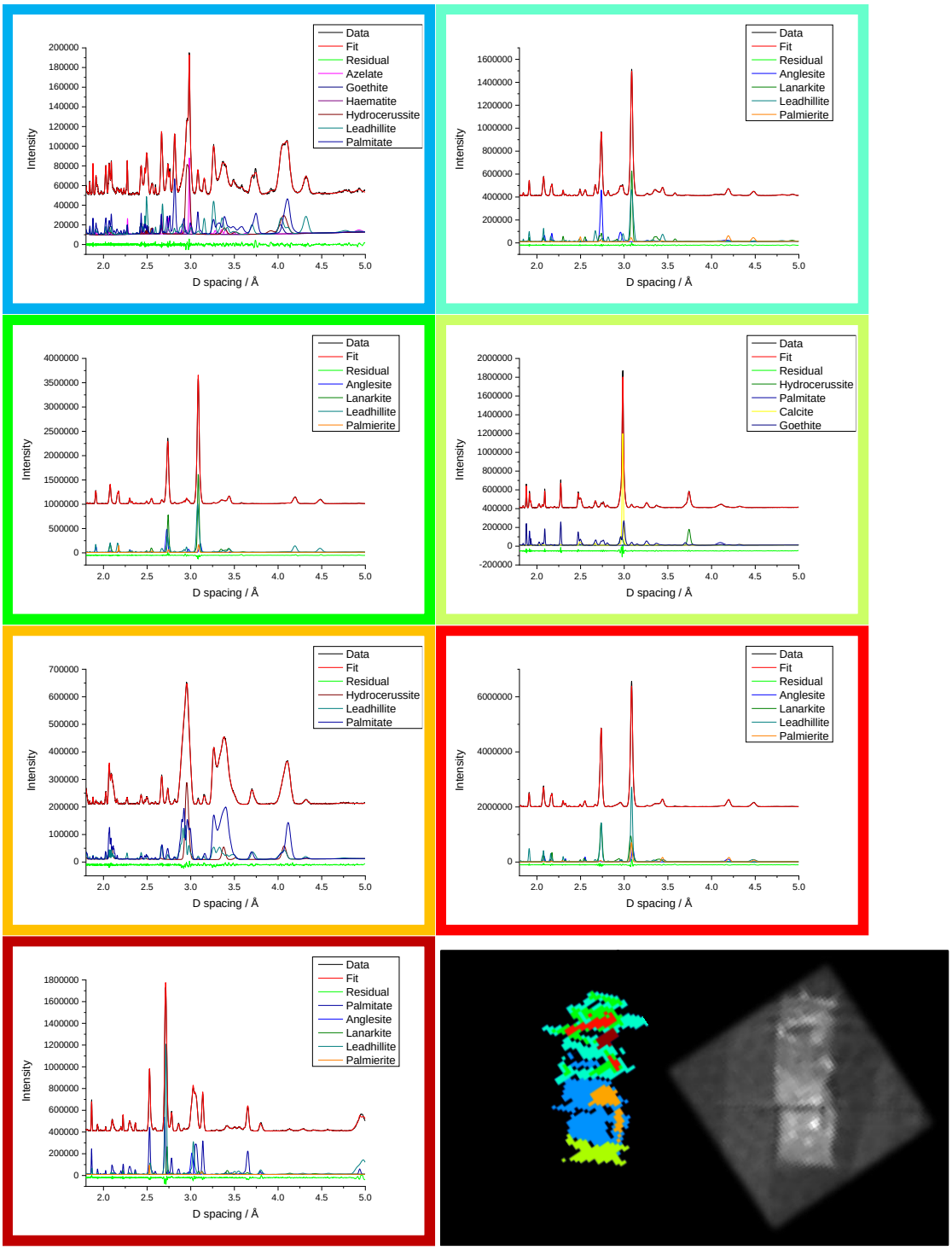

Figure S5: Cluster analysis of XRD-CT slice 3 (bottom middle), and absorption-CT (bottom right) of second tomogram location and diffraction patterns associated with each cluster (the colour of the box around the plot corresponds to the colour of the cluster in the XRD-CT image). Within each plot associated with a cluster, all phases have been assigned a unique colour: anglesite (light blue line), palmierite (orange line), lanarkite (green line), leadhillite (dark green line), calcite (yellow line), lead palmitate (blue line), hydrocerussite (brown line), goethite (dark blue line), haematite (purple line), lead azelate (pink line). Data (black line), fit (red line), residual (light green line). NB large single crystals present near the surface have caused significant streak artefacts that the filtering has not fully removed.

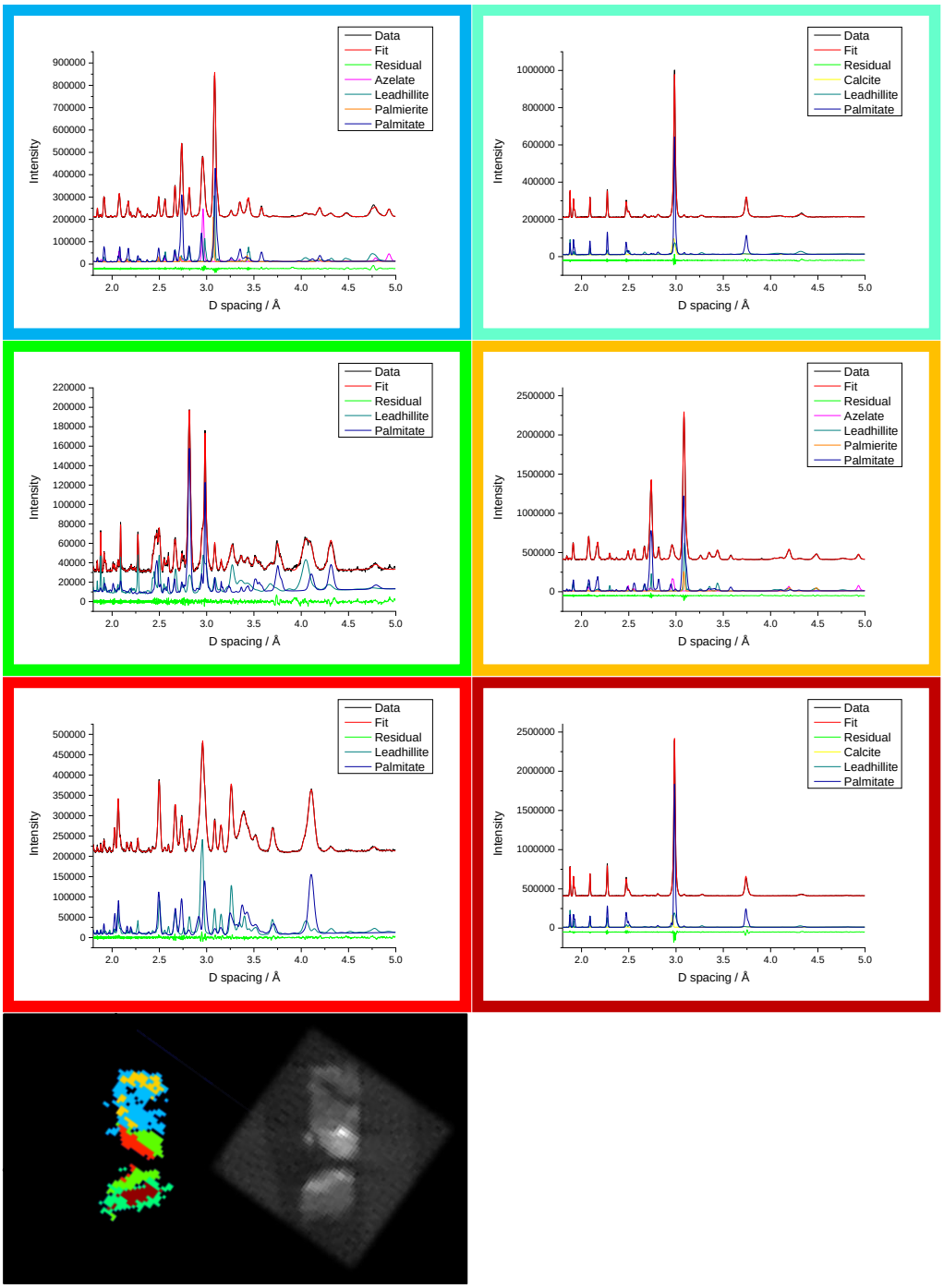

Figure S6: Cluster analysis of XRD-CT slice 3 (bottom left), and absorption-CT (bottom right) of second tomogram location and diffraction patterns associated with each cluster (the colour of the box around the plot corresponds to the colour of the cluster in the XRD-CT image). Within each plot associated with a cluster, all phases have been assigned a unique colour: anglesite (light blue line), palmierite (orange line), lanarkite (green line), leadhillite (dark green line), calcite (yellow line), lead palmitate (blue line), hydrocerussite (brown line), goethite (dark blue line), haematite (purple line), lead azelate (pink line). Data (black line), fit (red line), residual (light green line).

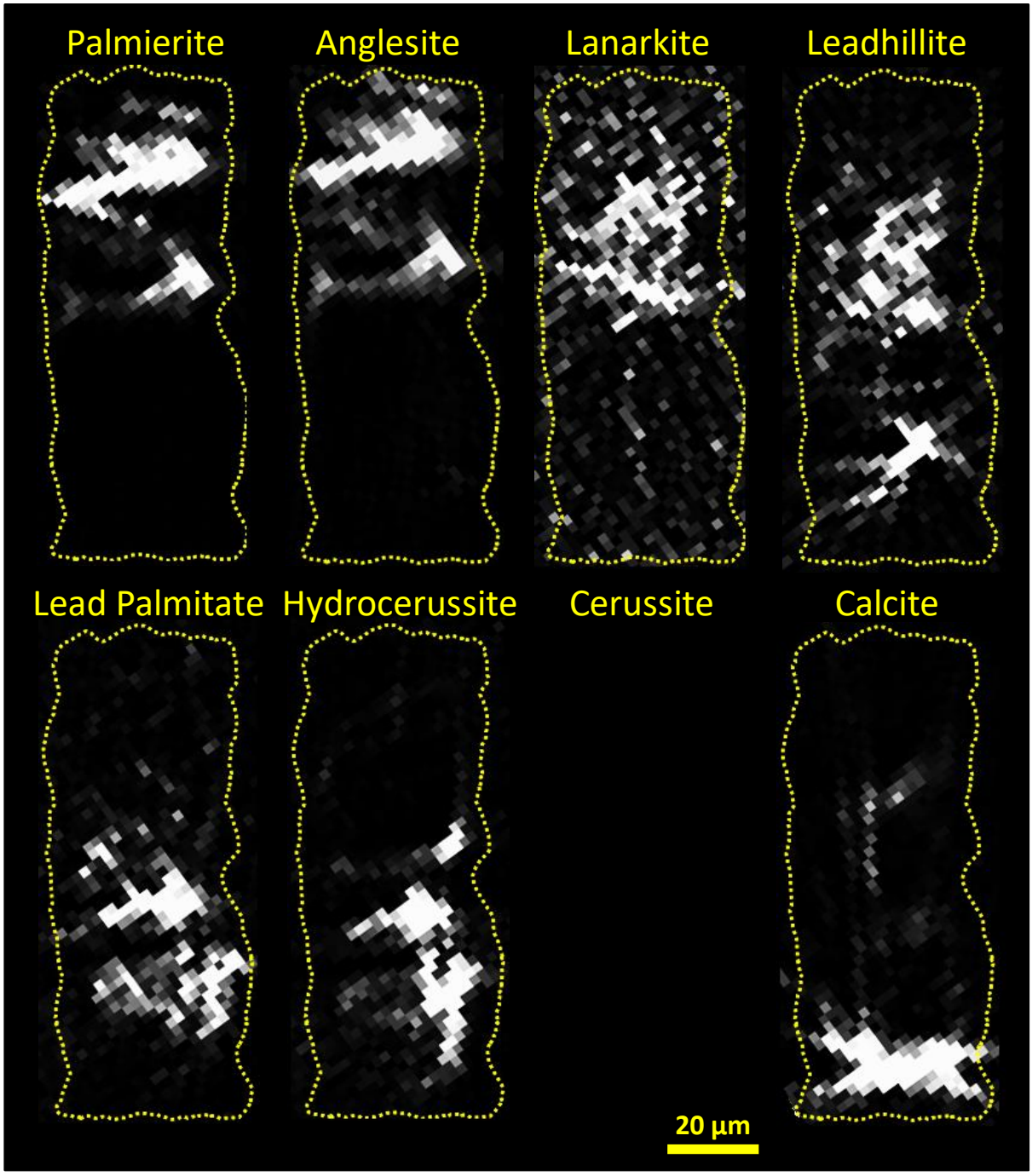

Figure S7: Maps of the location of each major Pb containing phase for the Rembrandt fragment (slice 2). Dashed yellow outline over each phase marks the approximate boundaries of the sample as defined by the absorption reconstruction, and act as a guide to identify the relative location of each phase within the sample. Where possible the major reflection has been used to create the map of the phase, however this is not always possible, and so in certain cases a less intense reflection was used, this resulted in higher background noise (e.g. lanarkite).

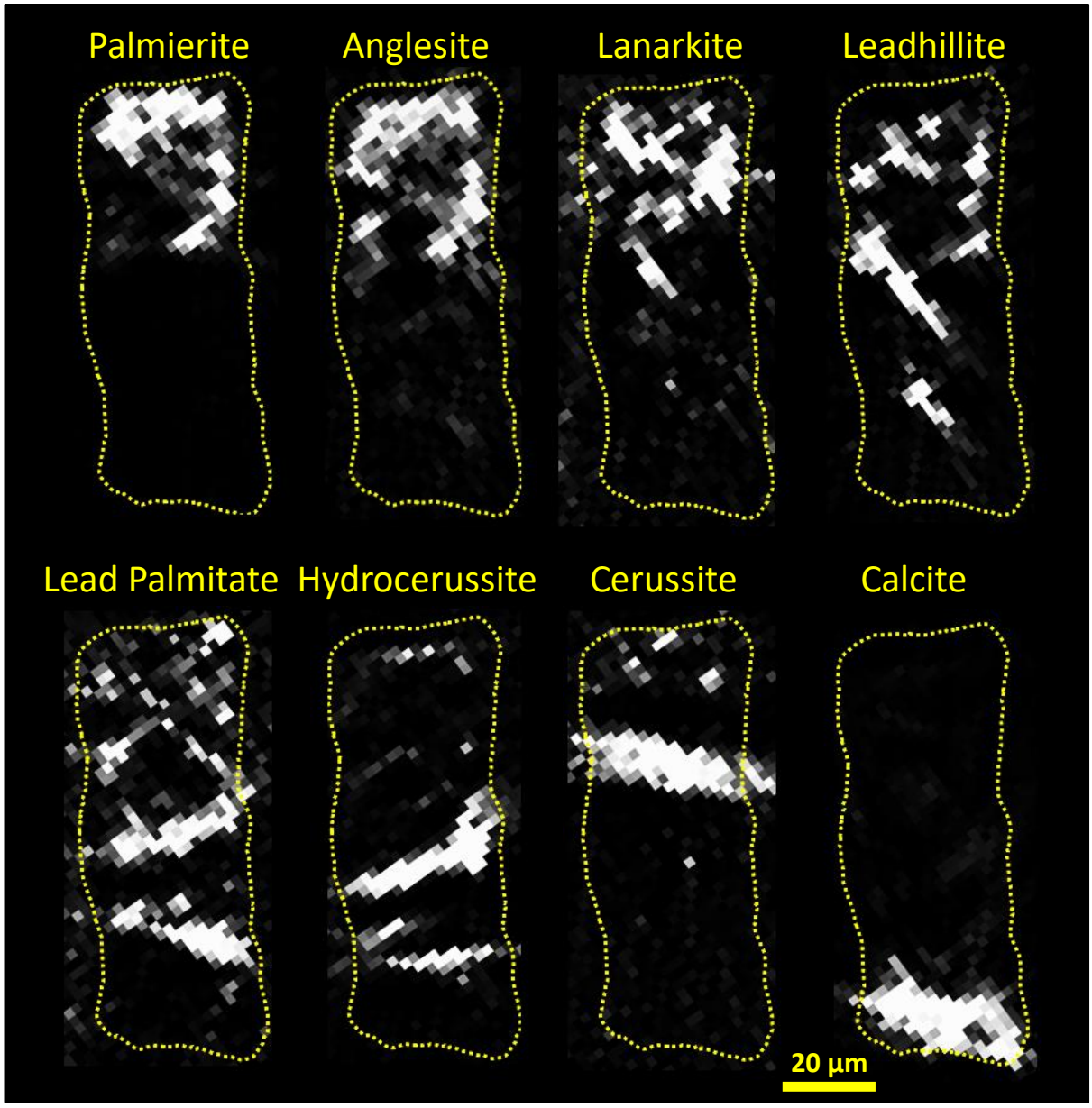

Figure S8: Maps of the location of each major Pb containing phase for the Rembrandt fragment (slice 3). Dashed yellow outline over each phase marks the approximate boundaries of the sample as defined by the absorption reconstruction, and act as a guide to identify the relative location of each phase within the sample. Where possible the major reflection has been used to create the map of the phase, however this is not always possible, and so in certain cases a less intense reflection was used, this resulted in higher background noise (e.g. lanarkite).

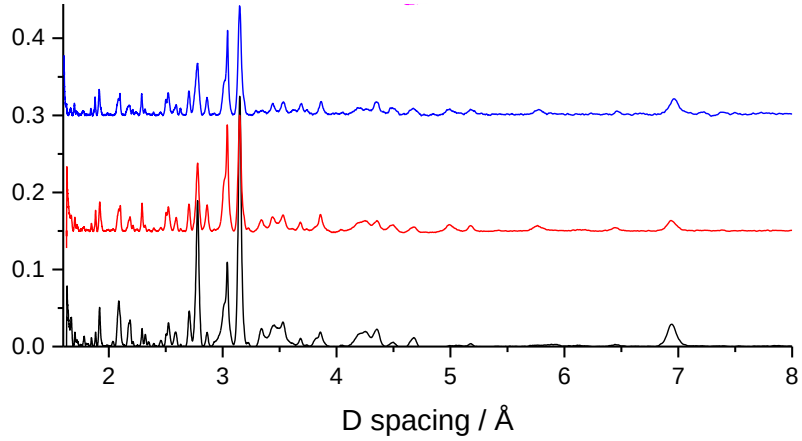

Figure S9 Summed diffraction patterns from XRD-CT slices 1 (black), 2 (red) and 3 (blue).

[1] J. F. W. Mosselmans, P. D. Quinn, A. J. Dent, S. A. Cavill, S. D. Moreno, A. Peach, P. J. Leicester, S. J. Keylock, S. R. Gregory, K. D. Atkinson and J. R. Rosell, *Journal of Synchrotron Radiation* **2009**, *16*, 818-824.
[2] a) R. C. Atwood, A. J. Bodey, S. W. T. Price, M. Basham and M. Drakopoulos, *Philosophical Transactions of the Royal Society of London A: Mathematical, Physical and Engineering Sciences* **2015**, *373*; b) A. D. Parsons, S. W. T. Price, N. Wadeson, M. Basham, A. M. Beale, A. W. Ashton, J. F. W. Mosselmans and P. D. Quinn, *Journal of Synchrotron Radiation* **2017**, *24*, 248-256; c) N. Wadeson and M. Basham, *CoRR* **2016**, *abs/1610.08015*.
[3] A. Vamvakeros, S. D. M. Jacques, M. Di Michiel, V. Middelkoop, C. K. Egan, R. J. Cernik and A. M. Beale, *Journal of Applied Crystallography* **2015**, *48*, 1943-1955.
[4] M. Lerotic, C. Jacobsen, T. Schäfer and S. Vogt, *Ultramicroscopy* **2004**, *100*, 35-57.
[5] A. Coelho in *Topas Version 4.2*, *Vol.* Coelho Software, Brisbane, **2007**.